# Visualization of arrestin recruitment by a G Protein-Coupled Receptor

**Arun K. Shukla**[#1,#], **Gerwin H. Westfield**[#2], **Kunhong Xiao**[#1], **Rosana I. Reis**[1], **Li-Yin Huang**[1], **Prachi Tripathi-Shukla**[1], **Jiang Qian**[1], **Sheng Li**[3], **Adi Blanc**[1], **Austin N. Oleskie**[2], **Anne M. Dosey**[2], **Min Su**[2], **Cui-Rong Liang**[4], **Ling-Ling Gu**[4], **Jin-Ming Shan**[4], **Xin Chen**[4], **Rachel Hanna**[5], **Minjung Choi**[9], **Xiao Jie Yao**[1], **Bjoern U. Klink**[1], **Alem W. Kahsai**[1], **Sachdev S. Sidhu**[5], **Shohei Koide**[6], **Pawel A. Penczek**[7], **Anthony A. Kossiakoff**[6], **Virgil L. Woods Jr**[3], **Brian K. Kobilka**[8,☉], **Georgios Skiniotis**[2,☉], and **Robert J. Lefkowitz**[1,9,10,☉]

[1]Department of Medicine, Duke University Medical Center, Durham, North Carolina 27710, USA

[2]Life Sciences Institute and Department of Biological Chemistry, University of Michigan Medical School, Ann Arbor, MI 48109, USA

[3]Department of Chemistry, University of California at San Diego, La Jolla, CA 92093, USA

[4]School of Pharmaceutical & Life Sciences, Changzhou University, Changzhou, Jiangsu 213164, China.

[5]Terrence Donnelly Centre for Cellular and Biomolecular Research, University of Toronto, Toronto, ON, Canada

[6]Department of Biochemistry and Molecular Biology, University of Chicago, Chicago, Illinois 60637, USA

[7]Department of Biochemistry and Molecular Biology, The University of Texas Medical School at Houston, Houston, TX 77054, USA

☉ Correspondence and requests for materials should be addressed to Robert J. Lefkowitz (lefko001@receptor-biol.duke.edu), Brian K. Kobilka (kobilka@stanford.edu) or Georgios Skiniotis (skinioti@umich.edu).
#current address is Department of Biological Sciences and Bioengineering, Indian Institute of Technology, Kanpur 208016, India.

8Department of Molecular and Cellular Physiology, Stanford University School of Medicine, 279 Campus Drive, Stanford, California 94305, USA

9Department of Biochemistry, Duke University Medical Center, Durham, North Carolina 27710, USA

10Howard Hughes Medical Institute, Duke University Medical Center, Durham, North Carolina 27710, USA

# These authors contributed equally to this work.

## Abstract

G Protein Coupled Receptors (GPCRs) are critically regulated by β-arrestins (βarrs), which not only desensitize G protein signaling but also initiate a G protein independent wave of signaling[1-5]. A recent surge of structural data on a number of GPCRs, including the $\beta_2$ adrenergic receptor ($\beta_2$AR)-G protein complex, has provided novel insights into the structural basis of receptor activation[6-11]. Lacking however has been complementary information on recruitment of βarrs to activated GPCRs primarily due to challenges in obtaining stable receptor-βarr complexes for structural studies. Here, we devised a strategy for forming and purifying a functional $\beta_2$AR-βarr1 complex that allowed us to visualize its architecture by single particle negative stain electron microscopy (EM) and to characterize the interactions between $\beta_2$AR and βarr1 using hydrogen-deuterium exchange mass spectrometry (HDXMS) and chemical cross-linking. EM 2D averages and 3D reconstructions reveal bimodal binding of βarr1 to the $\beta_2$AR, involving two separate sets of interactions, one with the phosphorylated carboxy-terminus of the receptor and the other with its seven-transmembrane core. Areas of reduced HDX together with identification of cross-linked residues suggest engagement of the finger loop of βarr1 with the seven-transmembrane core of the receptor. In contrast, focal areas of increased HDX indicate regions of increased dynamics in both N and C domains of βarr1 when coupled to the $\beta_2$AR. A molecular model of the $\beta_2$AR-βarr signaling complex was made by docking activated βarr1 and $\beta_2$AR crystal structures into the EM map densities with constraints provided by HDXMS and cross-linking, allowing us to obtain valuable insights into the overall architecture of a receptor-arrestin complex. The dynamic and structural information presented herein provides a framework for better understanding the basis of GPCR regulation by arrestins.

To facilitate the isolation of a stable $\beta_2$AR-βarr complex, we utilized a modified $\beta_2$AR construct with its carboxy-terminus replaced by that of the arginine vasopressin type 2 receptor (AVPR$_2$). This chimeric receptor ($\beta_2$V$_2$R) maintains pharmacological properties identical to the $\beta_2$AR, but it binds βarrs with higher affinity compared to wild-type $\beta_2$AR[12]. We co-expressed the $\beta_2$V$_2$R, βarr1 (1-393) and GRK2$^{CAAX}$ in insect cells followed by agonist stimulation and affinity purification through the FLAG-tagged receptor (Fig. 1a) However, since the isolation of a stable complex was still not feasible (Fig. 1b, lanes1,2), we explored enhancing its stability by adding Fab30, an antibody fragment that we previously reported to selectively recognize and stabilize the active conformation of βarr1[13]. Indeed, incubation of Fab30 with pre-formed complex in the membrane resulted in a robust purification of the $\beta_2$V$_2$R-βarr1 complex (Fig. 1b, lanes 5,6), whereas a non-specific Fab (referred to as Fab1) did not support complex stabilization (Fig.1b, lanes 3,4). Complex

isolation was only possible in response to an agonist (BI-167107) and not an inverse agonist (ICI-118551) (Fig. 1b, lanes 5,6). Furthermore, the efficiency of complex purification using this approach directly mirrors the pharmacological efficacy of the ligand used to stimulate the cells (Fig. 1c). While stimulation of cells with inverse agonists does not yield significant co-purification of βarr1, agonists robustly stabilize the complex and partial agonists yield co-purification of βarr1 at moderate levels. Moreover, the efficiency of complex formation also corresponds to the ligand occupancy of the receptor as reflected by the increasing amount of βarr1 co-purification with increasing agonist concentrations (Extended Data Fig. 1a,b). The direct correlation of ligand efficacy and occupancy with purification efficiency reflects that this approach yields a complex that depends on both activated receptor conformation and receptor phosphorylation. The purified $\beta_2V_2R$-βarr1-Fab30 complex also exhibited robust interaction with purified clathrin terminal domain compared to βarr1 alone, suggesting that βarr1 in this complex is in a physiologically relevant and functional conformation (Extended Data Fig. 2)[14-16]. Importantly, this strategy allowed preparative scale purification of a highly stable $\beta_2V_2R$-βarr1-Fab30 complex as assessed by analytical size exclusion chromatography (Fig. 1a, last panel, green trace and Extended Data Fig. 1c). In addition to the Fab30 stabilized $\beta_2V_2R$-βarr1 complex, we were also able to obtain equally stable $\beta_2V_2R$-βarr1 complexes using the single chain variable fragment of Fab30 (ScFv30) (Fig. 1a, last panel, blue trace).

The interaction of βarrs with activated GPCRs is proposed to involve two sequential steps[17]. First, the phosphorylated carboxy-terminus of activated GPCRs is thought to engage the N-domain of βarrs, a high affinity charge-charge interaction primarily mediated between the phosphates on the receptor tail and basic residues on βarrs[13,17]. This first engagement is hypothesized to facilitate activating conformational changes in βarr, leading in turn to additional interactions with the transmembrane core of the receptor[17]. To obtain dynamic structural information on the receptor-βarr complex, we carried out hydrogen-deuterium exchange mass spectrometry (HDXMS) analysis on the purified assembly[18,19]. In addition to the $\beta_2V_2R$-βarr1-Fab30 complex, we used the arginine vasopressin type 2 receptor carboxy-terminal phosphopeptide ($V_2$Rpp)-βarr1-Fab30 complex as a reference to extract specific information about the core interaction between the receptor and βarr1.

We observed a reduction in the hydrogen-deuterium exchange rate in the three major loops, the finger loop (55%), the middle loop (16%) and lariat loop (23%) of βarr1 when we compared the HDXMS profile of the $\beta_2V_2R$-βarr1-Fab30 complex with that of $V_2$Rpp-βarr1-Fab30 complex (Fig. 2 and Extended Data Figure 3a). Thus, these regions, and especially the finger loop, are likely to be buried (or have reduced solvent exposure) in the $\beta_2V_2R$-βarr1-Fab30 complex, most likely through an intricate engagement with the transmembrane receptor core. This finding is consistent with previous EPR studies on rhodopsin-arrestin interactions, which revealed a crucial involvement of the finger loop of arrestin with the core of rhodopsin[17,20-22]. Interestingly, several regions in both the N- and the C-domains of βarr1, in contrast, reveal enhanced hydrogen-deuterium exchange rates indicating that they become more dynamic upon interaction of βarr with the agonist bound phosphorylated receptor. This observation suggests that the core interaction between βarr1 and $\beta_2V_2R$ likely has long-range effects in βarr1 structure. Previous studies mapping interactions between GPCRs and arrestins suggested that receptors may also interact with

the broad concave surfaces of the N- and C-domains of arrestins[21,23-25]. However, peptides representing these surfaces are not fully represented in our HDXMS studies, thus limiting our ability to detect these interactions. We also note that our previously published high affinity agonist radioligand binding data on the T4L-$\beta_2$V$_2$R-$\beta$arr1-Fab30 complex in membranes, which provides a readout of the fully engaged $\beta$arr conformation, suggested that approximately 32% of the receptor is in a high affinity agonist binding state[13]. This indicates that our HDXMS data represents an average of two mixed complex populations, one with fully engaged $\beta$arr1 with the receptor and the other displaying partially engaged $\beta$arr1.

Our previous crystal structure of V$_2$Rpp bound activated $\beta$arr1 revealed a significant repositioning of the finger loop compared to the inactive $\beta$arr1, presumably primed to engage with the transmembrane core of the activated receptor[13]. To test this we carried out mass-spectrometry based mapping of the T4L-$\beta_2$V$_2$R-$\beta$arr1 interface using the homobifunctional, primary amine reactive chemical cross-linker DiSuccinimidyl Adipate (DSA). We found that Lys$^{77}$ on $\beta$arr1 (towards the distal end of the finger loop) cross-links with Lys$^{235}$ in the 3$^{rd}$ intracellular loop of the $\beta_2$AR (Extended Data Fig. 3b-e). These findings are in line with previously published biochemical and biophysical data suggesting an intricate interaction of the receptor core and the finger loop in arrestins. As an additional control for the close proximity of these residues, we created a series of mutants with single cysteine substitutions around Lys$^{235}$ in the amino terminal end of the 3$^{rd}$ intracellular loop of the $\beta_2$V$_2$R (amino acids 231-236) and in the finger loop around Lys$^{77}$ of $\beta$arr1 (amino acids 75-79) and evaluated the formation of disulphide trapped complexes in pairs of receptor and $\beta$arr1 mutants. Consistent with our chemical cross-linking data, cysteines engineered at position 235 of the receptor and at position 78 in $\beta$arr1 yielded the most robust disulphide trapped complex, suggesting a close proximity of these two residues in the complex (Extended Data Fig. 4). Taken together these findings demonstrate a direct interaction of the finger loop with the receptor core.

We next employed single particle EM to examine the architecture and conformational dynamics of $\beta_2$V$_2$R-$\beta$arr1 complexes. Due to the asymmetric nature and small size of these complexes (~150 kDa and ~125 kDa for the Fab and ScFv complexes, respectively) characterization attempts with cryo-EM were not successful and we thus applied negative stain EM that provides adequate contrast for alignment of small particle projections. This approach also enabled a direct comparison with our earlier negative stain EM analysis of the $\beta_2$AR-G$\alpha$s protein complex[9]. As in that work, here we used a T4 lysozyme fusion at the N-terminus of the receptor (referred as T4L-$\beta_2$V$_2$R) to provide a marker for the receptor orientation[9]. The negative stain EM visualization showed a monodisperse particle population (Fig. 3a, Extended Data Fig. 5) and we applied reference-free alignment and classification to obtain 2D averages of the complex.

The majority of averages of the $\beta_2$V$_2$R-$\beta$arr1-Fab30 complex revealed distinct projection profiles of an ovoid density, attributed to the receptor in partially flattened detergent micelle, with an attached T-like density attributed to the Fab30-$\beta$arr1 complex (Fig. 3b, Extended Data Fig. 6a). Comparisons with averages of the $\beta_2$V$_2$R-$\beta$arr1-ScFv30 complex identify the Fab30 density engaging the middle of $\beta$arr1, in agreement with our recent crystal structure

of βarr1-Fab30 co-crystallized with the $V_2Rpp$ (Fig. 3b, Extended data Fig. 6b). In this conformation βarr1 appears to hang off the receptor via a single point interaction presumably involving only the flexible $V_2Rpp$ fused on $β_2AR$. The flexible nature of this interaction is further supported by the variable receptor orientation in these averages, as judged by the T4L domain positioning. It is possible that the "hanging" arrestin conformation based on the $V_2Rpp$-βarr1 interaction represents a transient intermediate step in the recruitment process that has been stabilized by Fab30. Strikingly, we also observe a significant number of class averages representing ~37% of particles where βarr1 forms a much more extensive interface with the receptor, employing roughly the opposite face of the Fab30 binding region (Fig. 3b, lower panel). The observed fraction of particles displaying the extensive interface is in agreement with our previous radioligand binding results on the T4L-$β_2V_2R$-βarr1-Fab30 complex in membranes, which suggested approximately 32% of the receptor in a high affinity agonist binding state[13]. This observation also raised the possibility that βarr1 fully engages the receptor through a second set of weak interactions.

To stabilize this weak interaction, we developed an approach whereby the $β_2V_2R$-βarr1-Fab30/ScFv30 complex is cross-linked by exposure to a glutaraldehyde containing buffer zone while migrating through a size exclusion column (Extended Data Fig. 7a). This method facilitated near complete cross-linking of preformed complexes at relatively high concentrations and simultaneously enabled the isolation of highly monodisperse sample (Extended Data Fig. 7b,c, 8 and 9).

EM classification and averaging of the cross-linked $β_2V_2R$-βarr1-Fab30/ScFv30 complexes revealed distinct views of a uniform particle architecture, suggesting that cross-linking stabilized a single complex conformer (Fig. 3c). More importantly, the averages show that arrestin interacts extensively with the receptor in a configuration that appears very similar to the one observed in the smaller fraction (~37%) of the native complex. The conformational stabilizing action of the cross-linking is also evidenced by the consistent position of the T4L projection profile, in contrast to its variable positioning observed in averages of the native complex. To better characterize the $β_2V_2R$-βarr1 assembly, we employed the random conical-tilt approach[26] to calculate low resolution 3D maps (~29 Å) from selected classes of the cross-linked complex (Extended Data Fig. 10). The 3D reconstructions show distinct densities for the main complex components, in full agreement with our domain assignment in the 2D projections averages (Fig. 4a, Extended Data Fig. 10). The receptor containing region appears ovoid due to the large micelle "belt" characteristic of the LMNG detergent, as we also observed in the case of the $β_2AR$-Gαs complex[9]. A protrusion on one end of the receptor-micelle globular density represents the T4L domain that marks the receptor extracellular region. On the opposite side, the βarr1 density lies longitudinally on the receptor, engaging roughly the opposite side of the Fab30 interacting region. In this configuration, both βarr domains appear to engage the receptor but one of the domains lies mostly outside the interacting zone.

The HDXMS, chemical cross-linking and disulphide trapping data allowed us to constrain the modeling of the T4L-$β_2AR$ and βarr1-Fab30 crystal structures within the density of the EM 3D maps and generate a low-resolution model for the overall conformation of the $β_2AR$-βarr1 complex (Fig. 4b). This model can accommodate limited rotations and translations of

the individual crystal structures, which are also expected to undergo conformational changes upon complex formation. Lys[77] of βarr1 in our model is placed in close proximity to $\beta_2AR$ Lys[235] which is located at the end of a helical extension of TM5 in the $\beta_2AR$-$G\alpha_s$ complex[10]. This prompted us to use this structure to model the $\beta_2AR$-βarr1 complex. In our model, βarr1 forms an extensive interface with the receptor through its N-terminal domain involving interactions with the phosphorylated receptor tail and the insertion of the finger loop directly in the receptor core, involving the space between TM 3,5 and 6. We note that the finger loop insertion is likely associated with outward shifts in the positioning of TM helices 3, 5 and 6 and also helix 8. The middle and lariat loops of βarr1 are not participating in major interactions but reside close to the interface as suggested by their modest reduction in hydrogen-deuterium exchange rates observed by HDXMS (Fig. 2c). The relative positioning of these loops is also in agreement with previous EPR studies on visual arrestin in complex with activated and phosphorylated rhodopsin[20,21].

In regards to $\beta_2AR$, TM5 and the 3rd intracellular loop in this model locate above the concave β-sheet region of the N-terminal domain of βarr1. The placement of these receptor elements implies that the N-terminus of the $V_2Rpp$ cannot be in the position observed in the crystal structure of $V_2Rpp$-βarr1-Fab30[13], suggesting that the $V_2R$ carboxy-terminus in the $\beta_2V_2R$ chimeric receptor is mobile and repositions itself significantly upon βarr1 interaction with the receptor core. In contrast to the N-terminal domain, the C-terminal domain of βarr1 lies mostly outside the interaction zone, apart from the loop of residues 242-246 that is in interacting distance from the short α-helical segment connecting TM3 and TM4 of $\beta_2V_2R$. This observation is intriguing considering that mutation of the residues distal to the DRY motif (at the end of TM3) have been reported to directly affect βarr recruitment for a number of GPCRs including the $\beta_2AR$[27].

Our results suggest that arrestin likely employs a biphasic mechanism to engage the receptor (Fig. 4c). The first phase involves an interaction between the phosphorylated C-terminal tail of the receptor and the N-terminal domain of arrestin. Given the flexibility and the length of the C-terminal receptor tail, it is expected to act like a fishing line sampling a wide interaction space at a high rate. The second point of interaction appears weak and involves primarily the insertion of the finger loop within the receptor core, resulting in a longitudinal arrangement of arrestin on the receptor (Fig 4a,c). This arrangement would most certainly preclude GPCR engagement of G-protein heterotrimers, thereby blocking classical GPCR signaling and inducing desensitization. While it is not yet clear whether the single point interaction resulting in a "hanging" arrestin configuration has other physiological functions, it seems possible that these might involve recruitment and complex formation with components of the receptor endocytosis and signaling machinery such as clathrin and Gβγ.

## Online methods

### Reagents

Insect cell culture media and transfection kits to generate various virus stocks were purchased from Expression systems. Superdex 200 SEC columns were purchased from GE healthcare and detergents were purchased from Anatrace. EM grade glutaraldehyde solution and other general chemicals were purchased from Sigma.

## Protein expression and purification

T4L-$\beta_2$V$_2$R plasmid (with N-terminal fusion of T4 lysozyme) was generated by modifying the previously described T4L-$\beta_2$AR[6]. T4L-$\beta_2$V$_2$R was co-expressed with untagged bovine $\beta$arr1 (1-393) and untagged GRK2$^{CAAX}$ in *Sf*9 cells. 60-66h post-infection, cells were stimulated for 30 min (or indicated time) at 37°C with indicated ligand to induce receptor phosphorylation and ternary complex formation. Subsequently, cells were harvested, lysed in 20mM Hepes, pH 7.4, 150mM NaCl, 100nM-1uM ligand and protease inhibitors by douncing and purified Fab30/ScFv30 was added to this cell lysate. Following 1h incubation at room temperature, proteins were solubilized by adding detergent (0.5% LMNG or 1% DDM) and gentle stirring at room temperature for 1h. Solubilized material was purified on a FLAG M1 resin essentially using the protocol described for $\beta_2$AR purification previously[11]. In order to avoid potential protein aggregation at high concentration, free cysteines in the eluted proteins were blocked using iodoacetamide as described previously[11]. Proteins were concentrated using a 100 kDa Vivaspin or Millipore concentrator and loaded on to a preparative size exclusion column (Superdex 200, 16/600). The column was run at 0.3 ml/min and the column running buffer consists of 20mM Hepes, pH 7.4, 150mM NaCl, 100nM BI-167107, 0.01% LMNG, 100μM TCEP. Elution fractions corresponding to the complex peak were either pooled or used individually for further studies. Selection, characterization and purification of this Fab30 has been described previously[13].

## Biochemical and functional characterization of the complex

In order to pharmacologically validate this novel procedure, we stimulated the cells with multiple ligands (10μM) of varying efficacies (ranging from inverse agonists, partial agonists to full agonists). Subsequently, the cells were lysed, incubated with Fab30 and the complex was purified using FLAG M1 affinity resin. Purification of complex was assessed by the extent of $\beta$arr1 co-purified with the receptor. In order to further investigate agonist dependence of the complex formation, we assessed whether formation of this ternary complex through Fab30 stabilization follows ligand occupancy of the receptor. Cells were stimulated with varying doses of the agonist BI-167107 or Inverse agonist ICI-118551 at 37°C for 30 min. Subsequently, purification of the complex was performed as described above. Similarly, a time course of agonist and inverse agonist stimulation was carried out to identify the optimal time point to achieve maximal complex formation.

For stability analysis, the purified T4L-$\beta_2$V$_2$R-$\beta$arr1-Fab30 complex (1mg/mL) was either analyzed fresh after purification (reference sample, day 0) or incubated in the cold room and at room temperature for 4 days. Subsequently, the samples were analyzed by analytical size exclusion chromatography using a Superdex 200 (10/300) column. The column was run at 0.3 ml/min and the column running buffer consists of 20mM Hepes, pH 7.4, 150mM NaCl, 100nM BI-167,107, 0.01% LMNG, 100μM TCEP.

In order to validate the active conformation of $\beta$arr1 in the T4L-$\beta_2$V$_2$R-$\beta$arr1-Fab30 complex, we evaluated the ability of this complex to interact with purified clathrin terminal domain (heavy chain). The GST-clathrin-TD expression plasmid was a kind gift from Prof. Jeffrey Benovic and Dr. DongSoo Kang (Thomas Jefferson University). GST-clathrin-TD was expressed in *E. coli* using a previously published procedure[29] and immobilized on

glutathione sepharose beads. Subsequently, either the purified complex (in 20mM Hepes, 150mM NaCl, 0.01% LMNG, 100nM BI) or purified βarr1 (1-393) was added to the clathrin-TD and incubated at room temperature for 1h. The amount of complex used in this experiment was normalized to contain equivalent amount of βarr1 as in βarr1 alone sample in order to directly compare the extent of clathrin interaction. Subsequently, the beads were washed 3 times with the same buffer as above and proteins were eluted using the SDS-gel loading buffer. The samples were analyzed by Western blotting using anti-βarr1 antibody and anti-clathrin antibody (BD Biosciences).

### Conversion of Fab30 in to ScFv30

In order to convert the Fab30 in to an ScFv, the variable domains of the light chain and the heavy chain were joined through a flexible linker (GTTAASGSSGGSSSGA) using standard PCR amplification and cloning techniques. The resulting sequence of the ScFv30 is as follows (linker sequence is underlined and highlighted in bold):

MKKNIAFLLASMFVFSIATNAYASDIQMTQSPSSLSASVGDRVTITCRASQSVSSAV AW
YQQKPGKAPKLLIYSASSLYSGVPSRFSGSRSGTDFTLTISSLQPEDFATYYCQQYKY V
PVTFGQGTKVEIK**GTTAASGSSGGSSSGA**EVQLVESGGGLVQPGGSLRLSCAASGF N
VYSSSIHWVRQAPGKGLEWVASISSYYGYTYYADSVKGRFTISADTSKNTAYLQMN SX RAEDTAVYYCARSRQFWYSGLDYWGQGTLVTVSSAHHHHHH.

ScFv30 was expressed using the same protocol as Fab30. It was either purified on Ni-NTA resin or used directly as periplasmic extract to stabilize the T4L-$\beta_2$V$_2$R-βarr1 complex.

### Glutaraldehyde cross-linking of the pre-formed complex

In order to mildly cross-link the complex, an "on-column" cross-linking method was used. First, a bolus of glutaraldehyde was injected to a pre-equilibrated Superdex 200 (10/300 global in 20mM Hepes, pH 7.4, 150mM NaCl, 0.01% LMNG, 100nM BI-167107) column and run at 0.25 ml/min for 20 min (i.e. a total of 5ml buffer). Subsequently, the column flow was paused, and the injection loop was flushed using buffer followed by injection of purified complex (200μl volume, at 5-10 μM concentration). Subsequently, the column was run at 0.25 ml/min and 0.3 ml fractions were collected. Cross-linking efficiency was visualized by running the individual fractions on a 4-20% SDS gel, followed by staining with "SimplyBlue" stain. Various concentrations of glutaraldehyde were tested in order to identify an optimal concentration (0.25% in this case) that yields maximal cross-linking efficiency and minimal protein aggregation.

## Hydrogen-Deuterium Exchange Mass Spectrometry (HDXMS)

### Fragmentation tuning for βarr1

We first performed fragmentation tuning experiments in order to optimize experimental conditions to achieve the best peptide fragmentation pattern for βarr1. In brief, 3 μL of βarr1

protein solution was diluted with 9 μL of a buffer containing 150mM NaCl, 8.3mM Tris-HCl, pH7.2 in $H_2O$ and then divided into equal sized aliquots. Each aliquot was mixed individually with 18 μL of a series of quench solutions containing 0.8% formic acid, 16.6% glycerol, and various concentrations of GuHCl (ranging from 0.05M to 4M) and TCEP (ranging from 0.015M to 0.5M). The protein-buffer-quench solution mixtures were incubated at 0°C for 1 minute, frozen on dry ice and then stored at −80 °C until subjected to on-line pepsin digestion and LC/MS analysis. Protein fragmentation maps under different conditions were generated and compared. The condition that produced the best peptide fragmentation pattern (the best coverage along the amino acid sequence, the most number of fragments, and highest number of high quality peptides) was used for all the HDXMS experiments described in this study.

### Hydrogen-deuterium exchange experiments

The $V_2Rpp$-βarr1-Fab30 and T4L-$β_2V_2R$-βarr1-Fab30 complexes were prepared as described above. Free βarr1 protein was used as a control. For each protein complex, three sets of samples were prepared: 1) non-deuterated (ND), 2) fully deuterated (FD), and 3) time-dependent on-exchange samples. A protein: buffer: quench solution ratio of 1:3:6 (volume) was used for all sample preparations. The FD sample sets were prepared by mixing protein samples with $D_2O$ buffer (0.8% Formic acid in 100% $D_2O$) and incubated at room temperature for 12 hours before quenching. The ND sample sets were prepared using a similar procedure with $H_2O$ buffer (150mM NaCl, 8.3 mM Tris-HCl, pH7.2 in $H_2O$) without the incubation step. The on-exchange sample sets were prepared by adding 3 volumes of $D_2O$ buffer (150mM NaCl, 8.3 mM Tris-HCl, pH7.2 in $D_2O$) at 0°C and incubating for varying time-points (10s, $10^2$s, $10^3$s, $10^4$s and $10^5$s). Six volumes of ice-cold quench solution was then added to each sample, followed by snap-freezing on dry ice and stored at −80°C.

### On-line pepsin digestion, LC/MS analysis and data processing

Samples prepared above were thawed right before the on-line pepsin digestion at 0°C using a cryogenic autosampler and immediately passed over an immobilized porcine pepsin column (16 μL bed volume). Peptide fragments were collected contemporaneously on a $C_{18}$ trap column desalting, separated by a Magic $C_{18}AQ$ column using a linear gradient of acetonitrile from 6.4% to 38.4% over 30 min, and followed by LC/MS analysis using an Orbitrap Elite mass spectrometer (Thermo Scientific). Both MS1 and MS2 spectra were collected using data-dependent acquisition mode. Peptide identification was performed using LC/MS data sets collected from ND samples and SEQUEST database search engine using Proteome Discoverer (Thermo Fisher Sci). The SEQUEST database search results were submitted to DXMS Explorer (Version 2.0, Sierra Analytics Inc.), filtered using several threshold parameters to create an initial peptide pool. The quality of the MS1 data for each filtered peptide was then checked by assigning an initial quality score by DXMS Explorer software, followed by a quality control process which included manual investigation of peak isotopic envelope and adjusting/improving the quality score. Only peptides with high quality in the MS1 spectra were kept in the final peptide pool. The retention times and *m/z* ranges of each peptide from the final peptide pool was manually verified and adjusted across all LC/MS data sets from on-exchange samples and FD samples

to ensure that DXMS Explorer had selected the correct peptide for all experiments. Results from FD samples were used to monitor the back-exchange rates during on-line pepsin digestion and LC/MS analysis. The centroids of isotopic envelopes of non-deuterated, partially deuterated and fully deuterated peptides were measured using DXMS Explorer, and then converted to deuteration level with corrections for back-exchange. A deuterium accumulation plot was created for each peptide as a further quality check and data refinement process. Rainbow maps were generated and DXMS data comparison was performed using different macros in Excel.

## Chemical cross-linking and mass spectrometry

### Chemical cross-linking reaction

In order to identify a potential interaction interface of the $\beta_2V_2R$ and $\beta arr1$, we performed chemical cross-linking experiments on the pre-formed T4L-$\beta_2V_2R$-$\beta arr1$-Fab30 complex. To facilitate the identification of cross-linked peptides, we used an equimolar mixture of light ($^{12}$C6) and heavy ($^{13}$C6) DiSuccinimidyl Adipate (DSA, a homobifunctional amine-reactive cross-linker, spacer arm=7.7 angstrom) to cross-link the complex. The cross-linked peptides were characterized with "doublet" peak signatures in mass spectra. The T4L-$\beta_2V_2R$-$\beta arr1$-Fab30 complex was prepared in buffer containing 20mM HEPES, 150mM NaCl, 0.01% LMNG, 100nM BI, 100uM TCEP. Cross-linker solution was freshly prepared in DMSO at a concentration of 10 mM. For the cross-linking reaction, 100-fold excess of DSA-$^{12}$C6:DSA-$^{13}$C6 equimolar mixture was added to the T4L-$\beta_2V_2R$-$\beta arr1$-Fab30 complex solution and incubated for 30 min at 25 °C. Unreacted cross-linker was quenched by incubation with 100 mM ammonium bicarbonate for 20 min. The cross-linked T4L-$\beta_2V_2R$-$\beta arr1$-Fab30 complex was separated by SDS-PAGE, and the corresponding protein band was in-gel digested overnight at 37 °C with trypsin at a final concentration of 10 ng/μL and subjected to LC/MS analysis as described below.

### LC/MS analysis and cross-linked peptide identification

LC/MS analyses were performed on a LTQ Orbitrap XL mass spectrometer (Thermo Scientific) with a Finnigan Nanospray II electrospray ionization source. Tryptic peptides were injected onto a 75 μm×150 mm BEH C18 column (particle size 1.7 μm, Waters) and separated using a Waters nano ACQUITY Ultra Performance LC™ (UPLC™) System (Waters, Milford, MA). The LTQ Orbitrap XL was operated in the data dependent mode using the TOP10 strategy[30]. In brief, each scan cycle was initiated with a full MS scan of high mass accuracy 375–1800 $m/z$; acquired in the Orbitrap XL at $6\times10^4$ resolution setting and automatic gain control (AGC) target of $10^6$, which was followed by MS/MS scans (AGC target 5000; threshold 3000) in the linear ion trap on the 10 most abundant precursor ions. Selected ions were dynamically excluded for 30 s. Singly charged ions were excluded from MS/MS analysis. The LC/MS/MS data was processed and analyzed by pLink software[31]. In brief, acquired raw data from LTQ Orbitrap XL mass spectrometer was first converted to mgf files using Mascot Distiller or Proteowizard 3.0 and saved under a pLink master directory, where a composite database containing protein sequences of T4L-$\beta_2V_2R$, $\beta arr1$ and Fab30 in FASTA format is also stored. In the pLink configuration file, both the names and paths of the mgf and database file were indicated correspondingly. The total

numbers of fixed modifications was set to 1 for cysteine carbamidomethylation. The name and number of cross-linkers used in the experiment were indicated as well in the configuration file. The filter for precursor mass accuracy was set to ± 10 ppm. After pLink analysis, identified cross-linked peptides were manually inspected in the raw file for the appearance of a pair of doublet MS peaks.

### Disulphide trapping of $\beta_2V_2R$ and βarr1 complex

Cysteine mutants of the $\beta_2V_2R$ and βarr1 were co-expressed in HEK-293 cells. 48h post-transfection, cells were stimulated with $\beta_2AR$ agonist Isoproterenol (10μM) and treated with $H_2O_2$ (1mM) at different time points to induce the formation of disulfide bond and trap the complex. Cells were washed and lysed in lysis buffer (50mM Hepes, 250mM NaCl, pH 7.4, 2 mM EDTA, 10% glycerol, 0.5% NP40, 1mM NaV, 57mM NaF, EDTA free Complete protease inhibitor). Cell lysates were used for anti-FLAG antibody immunoprecipitation (N-terminal FLAG tagged $\beta_2V_2$). Beads were washed and eluted proteins were separated by SDS-PAGE followed by detection using Western blotting. Expression levels of the receptor and βarr1 mutants were measured by radioligand binding and Western blotting, respectively. Densitometry analysis of the βarr1 bands was done using ImageJ software.

### Specimen preparation and EM imaging of negative stained samples

T4L-$\beta_2V_2R$-βarr1-Fab30/ScFv30 complex was prepared for electron microscopy using the conventional negative staining protocol[32], and imaged at room temperature with a Tecnai T12 electron microscope operated at 120 kV using low-dose procedures. Images were recorded at a magnification of 71,138x and a defocus value of ~1.5μm on a Gatan US4000 CCD camera. All images were binned (2 × 2 pixels) to obtain a pixel size of 4.16 Å on the specimen level. Particles were manually excised using Boxer [part of the EMAN 1.9 software suite] [33] apart from tilt pairs (0° and 60°) where particles were selected using WEB[34].

### 2D classification and 3D reconstructions of negative stained T4L-$\beta_2V_2R$-βarr-Fab30(ScFv30) complex

2D reference-free alignment and classification of particle projections was performed using ISAC[28]. 16,286 0° particle projections of native T4L-$\beta_2V_2R$-βarr-Fab30 complex and 13,703 0° projections of native T4L-$\beta_2V_2R$-βarr-ScFv30 complex were subjected to ISAC producing 186 classes accounting for 9,193 particle projections and 145 classes accounting for 8,127 projections, respectively. 14,109 0° particle projections of cross-linked T4L-$\beta_2V_2R$-βarr-ScFv30 complex and 13,106 0° projections of cross-linked T4L-$\beta_2V_2R$-βarr1-Fab30 complex were subjected to ISAC producing 111 classes accounting for 8,011 particle projections and 149 classes accounting for 8,127 projections, respectively. To determine the particle distribution of native T4L-$\beta_2V_2R$-βarr1-Fab30 conformations, each class average was designated as "tight", "loose" or "unassigned" and the number of projections contributing to the class averages for each designation were added to calculate percentages.

For native and cross-linked Fab30 complexes the random conical tilt technique[26] was used to calculate a first back projection map from individual classes using the 60° tilted particle projections. After angular refinement of the 60° projections, untilted particle projections

were added to the dataset and the images were subjected to another cycle of refinement. For final reconstructions, particle projections from similar class averages were pooled together, corrected for contrast transfer function (CTF) according to local defocus values obtained by CTFTILT[35] and subjected to further refinement and reconstruction in FREALIGN[36]. 2,825 particle projections from 0° and 60° images contributed to the cross-linked T4L-$\beta_2V_2R$-βarr1-Fab30 complex reconstruction. 2,196 particle projections from 0° and 60° images contributed to the native T4L-$\beta_2V_2R$-βarr1-Fab30 3D reconstruction. The resolution for each map was determined by the conventional Fourier Shell Correlation (FSC) approach at FSC=0.5 (Extended Data Figure 10).

## Molecular modeling

For modeling the T4L-$\beta_2V_2R$-βarr1-Fab30 complex we used the crystal structure of T4L-$\beta_2AR$ receptor from the T4L-$\beta_2AR$-Gαs complex (3SN6)[6] and the crystal structure of $V_2Rpp$-βarr1-Fab30 (4JQI). Due to the low resolution of the EM map and the presence of the significant detergent micelle density surrounding the receptor region all docking operations within the EM maps were performed manually with visual inspection of best fit while taking into account additional constraints from cross-linking and HDXMS data. The Fab30 and T4L structures were independently shifted from the original position in the corresponding crystal structures to obtain an improved fit into the EM density map, reflecting both, the flexible nature of their association with βarr1 and $\beta_2AR$, respectively, and a partial deformation of the complex on the carbon support of the EM grid.

## Acknowledgments

## References/Methods-only references

1. Pierce KL, Lefkowitz RJ. Classical and new roles of beta-arrestins in the regulation of G-protein-coupled receptors. Nat Rev Neurosci. 2001; 2:727–733. doi:10.1038/35094577. [PubMed: 11584310]

2. Shukla AK, Xiao K, Lefkowitz RJ. Emerging paradigms of beta-arrestin dependent seven transmembrane receptor signaling. Trends Biochem Sci. 2011; 36:457–469. doi:10.1016/j.tibs. 2011.06.003. [PubMed: 21764321]

3. Lefkowitz RJ, Shenoy SK. Transduction of receptor signals by beta-arrestins. Science. 2005; 308:512–517. doi:10.1126/science.1109237. [PubMed: 15845844]

4. Pierce KL, Premont RT, Lefkowitz RJ. Seven-transmembrane receptors. Nat Rev Mol Cell Biol. 2002; 3:639–650. doi:10.1038/nrm908. [PubMed: 12209124]

5. DeWire SM, Ahn S, Lefkowitz RJ, Shenoy SK. Beta-arrestins and cell signaling. Annu Rev Physiol. 2007; 69:483–510. doi:10.1146/annurev.ph.69.013107.100021. [PubMed: 17305471]

6. Rasmussen SG, et al. Crystal structure of the beta2 adrenergic receptor-Gs protein complex. Nature. 2011; 477:549–555. doi:10.1038/nature10361. [PubMed: 21772288]

7. Weis WI, Kobilka BK. Structural insights into G-protein-coupled receptor activation. Curr Opin Struct Biol. 2008; 18:734–740. doi:10.1016/j.sbi.2008.09.010. [PubMed: 18957321]

8. Rosenbaum DM, Rasmussen SG, Kobilka BK. The structure and function of G protein-coupled receptors. Nature. 2009; 459:356–363. doi:10.1038/nature08144. [PubMed: 19458711]

9. Westfield GH, et al. Structural flexibility of the G alpha s alpha-helical domain in the beta2-adrenoceptor Gs complex. Proceedings of the National Academy of Sciences of the United States of America. 2011; 108:16086–16091. doi:10.1073/pnas.1113645108. [PubMed: 21914848]

10. Rasmussen SG, et al. Crystal structure of the human beta2 adrenergic G-protein coupled receptor. Nature. 2007; 450:383–387. doi:10.1038/nature06325. [PubMed: 17952055]

11. Rasmussen SG, et al. Structure of a nanobody-stabilized active state of the beta(2) adrenoceptor. Nature. 2011; 469:175–180. doi:10.1038/nature09648. [PubMed: 21228869]

12. Oakley RH, Laporte SA, Holt JA, Caron MG, Barak LS. Differential affinities of visual arrestin, beta arrestin1, and beta arrestin2 for G protein-coupled receptors delineate two major classes of receptors. The Journal of biological chemistry. 2000; 275:17201–17210. doi:10.1074/jbc.M910348199. [PubMed: 10748214]

13. Shukla AK, et al. Structure of active beta-arrestin-1 bound to a G-protein-coupled receptor phosphopeptide. Nature. 2013; 497:137–141. doi:10.1038/nature12120. [PubMed: 23604254]

14. Goodman OB Jr. et al. Beta-arrestin acts as a clathrin adaptor in endocytosis of the beta2-adrenergic receptor. Nature. 1996; 383:447–450. doi:10.1038/383447a0. [PubMed: 8837779]

15. Nobles KN, Guan Z, Xiao K, Oas TG, Lefkowitz RJ. The active conformation of beta-arrestin1: direct evidence for the phosphate sensor in the N-domain and conformational differences in the active states of beta-arrestins1 and -2. The Journal of biological chemistry. 2007; 282:21370–21381. doi:10.1074/jbc.M611483200. [PubMed: 17513300]

16. Xiao K, Shenoy SK, Nobles K, Lefkowitz RJ. Activation-dependent conformational changes in {beta}-arrestin 2. The Journal of biological chemistry. 2004; 279:55744–55753. doi:10.1074/jbc.M409785200. [PubMed: 15501822]

17. Gurevich VV, Gurevich EV. The molecular acrobatics of arrestin activation. Trends in pharmacological sciences. 2004; 25:105–111. doi:10.1016/j.tips.2003.12.008. [PubMed: 15102497]

18. Chung KY, et al. Conformational changes in the G protein Gs induced by the beta2 adrenergic receptor. Nature. 2011; 477:611–615. doi:10.1038/nature10488. [PubMed: 21956331]

19. Konermann L, Pan J, Liu YH. Hydrogen exchange mass spectrometry for studying protein structure and dynamics. Chemical Society reviews. 2011; 40:1224–1234. doi:10.1039/c0cs00113a. [PubMed: 21173980]

20. Kim M, et al. Conformation of receptor-bound visual arrestin. Proceedings of the National Academy of Sciences of the United States of America. 2012; 109:18407–18412. doi:10.1073/pnas.1216304109. [PubMed: 23091036]

21. Hanson SM, et al. Differential interaction of spin-labeled arrestin with inactive and active phosphorhodopsin. Proceedings of the National Academy of Sciences of the United States of America. 2006; 103:4900–4905. doi:10.1073/pnas.0600733103. [PubMed: 16547131]

22. Zhuang T, et al. Involvement of distinct arrestin-1 elements in binding to different functional forms of rhodopsin. Proceedings of the National Academy of Sciences of the United States of America. 2013; 110:942–947. doi:10.1073/pnas.1215176110. [PubMed: 23277586]

23. Gimenez LE, Vishnivetskiy SA, Baameur F, Gurevich VV. Manipulation of very few receptor discriminator residues greatly enhances receptor specificity of non-visual arrestins. The Journal of biological chemistry. 2012; 287:29495–29505. doi:10.1074/jbc.M112.366674. [PubMed: 22787152]

24. Gurevich VV, Gurevich EV. Structural determinants of arrestin functions. Progress in molecular biology and translational science. 2013; 118:57–92. doi:10.1016/B978-0-12-394440-5.00003-6. [PubMed: 23764050]

25. Lohse MJ, Hoffmann C. Arrestin interactions with g protein-coupled receptors. Handbook of experimental pharmacology. 2014; 219:15–56. doi:10.1007/978-3-642-41199-1_2. [PubMed: 24292823]

26. Radermacher M, Wagenknecht T, Verschoor A, Frank J. Three-dimensional reconstruction from a single-exposure, random conical tilt series applied to the 50S ribosomal subunit of Escherichia coli. Journal of microscopy. 1987; 146:113–136. [PubMed: 3302267]

27. Kim KM, Caron MG. Complementary roles of the DRY motif and C-terminus tail of GPCRS for G protein coupling and beta-arrestin interaction. Biochemical and biophysical research communications. 2008; 366:42–47. doi:10.1016/j.bbrc.2007.11.055. [PubMed: 18036556]

28. Yang Z, Fang J, Chittuluru J, Asturias FJ, Penczek PA. Iterative stable alignment and clustering of 2D transmission electron microscope images. Structure. 2012; 20:237–247. doi:10.1016/j.str. 2011.12.007. [PubMed: 22325773]

29. Kang DS, et al. Structure of an arrestin2-clathrin complex reveals a novel clathrin binding domain that modulates receptor trafficking. The Journal of biological chemistry. 2009; 284:29860–29872. doi:10.1074/jbc.M109.023366. [PubMed: 19710023]

30. Haas W, et al. Optimization and use of peptide mass measurement accuracy in shotgun proteomics. Molecular &amp; cellular proteomics : MCP. 2006; 5:1326–1337. doi:10.1074/mcp.M500339-MCP200. [PubMed: 16635985]

31. Yang B, et al. Identification of cross-linked peptides from complex samples. Nature methods. 2012; 9:904–906. doi:10.1038/nmeth.2099. [PubMed: 22772728]

32. Ohi M, Li Y, Cheng Y, Walz T. Negative Staining and Image Classification - Powerful Tools in Modern Electron Microscopy. Biological procedures online. 2004; 6:23–34. doi:10.1251/bpo70. [PubMed: 15103397]

33. Ludtke SJ, Baldwin PR, Chiu W. EMAN: semiautomated software for high resolution single-particle reconstructions. Journal of structural biology. 1999; 128:82–97. doi:10.1006/jsbi. 1999.4174. [PubMed: 10600563]

34. Frank J, et al. SPIDER and WEB: processing and visualization of images in 3D electron microscopy and related fields. Journal of structural biology. 1996; 116:190–199. doi:10.1006/jsbi. 1996.0030. [PubMed: 8742743]

35. Mindell JA, Grigorieff N. Accurate determination of local defocus and specimen tilt in electron microscopy. Journal of structural biology. 2003; 142:334–347. [PubMed: 12781660]

36. Grigorieff N. FREALIGN: high-resolution refinement of single particle structures. Journal of structural biology. 2007; 157:117–125. doi:10.1016/j.jsb.2006.05.004. [PubMed: 16828314]
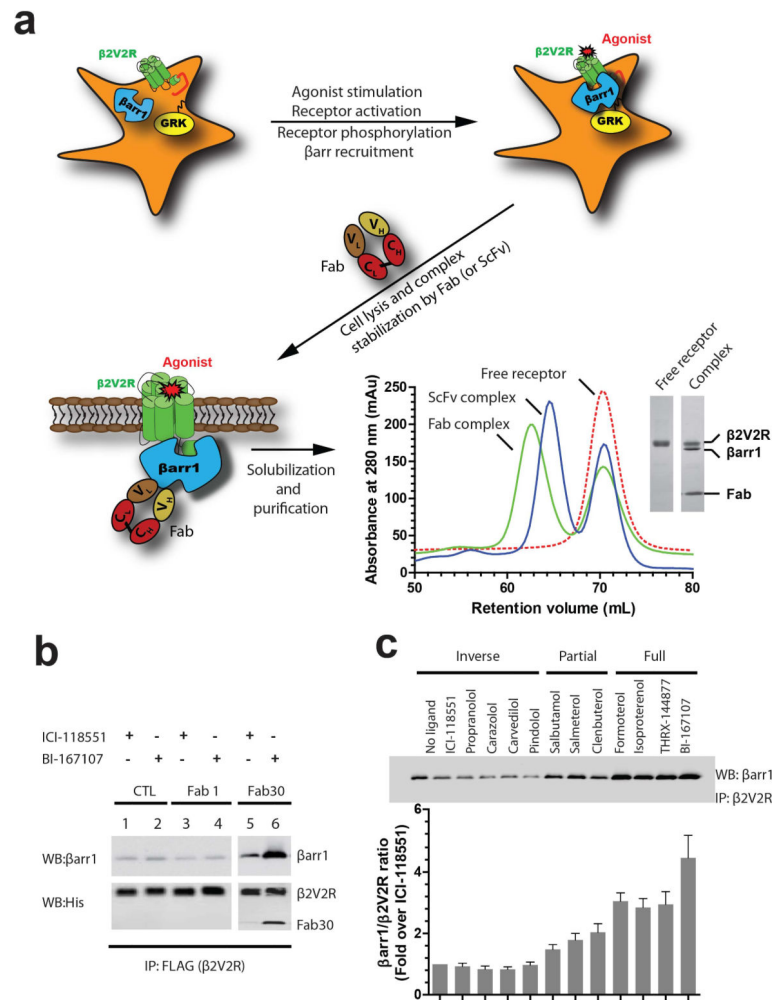
**Figure 1. Formation and functional characterization of a stable agonist-$\beta_2V_2R$-$\beta$arr1 signaling complex**

**a.** Schematic flowchart of a novel purification strategy to isolate $\beta_2V_2R$-$\beta$arr1-Fab30 complex and large scale production and separation of agonist-$\beta_2V_2R$-$\beta$arr1-Fab30/ScFv30 complex from the free receptor by size exclusion chromatography (Superdex 200, 16/600 prep grade). T4 lysozyme sequence is attached at the N-terminus of the $\beta_2AR$. **b.** Isolation of $\beta_2V_2R$-$\beta$arr1 complex requires Fab30 and it is agonist dependent. Cells were stimulated either with inverse agonist (ICI-118551) or agonist (BI-167107) followed by incubation with or without Fab and subsequent purification on FLAG M1 beads. **c.** Formation of $\beta_2V_2R$-$\beta$arr1-Fab30 complex follows ligand efficacy. Formation of the complex in response to inverse agonists, partial agonists and full agonists is shown. The data is representative of 7 independent experiments.
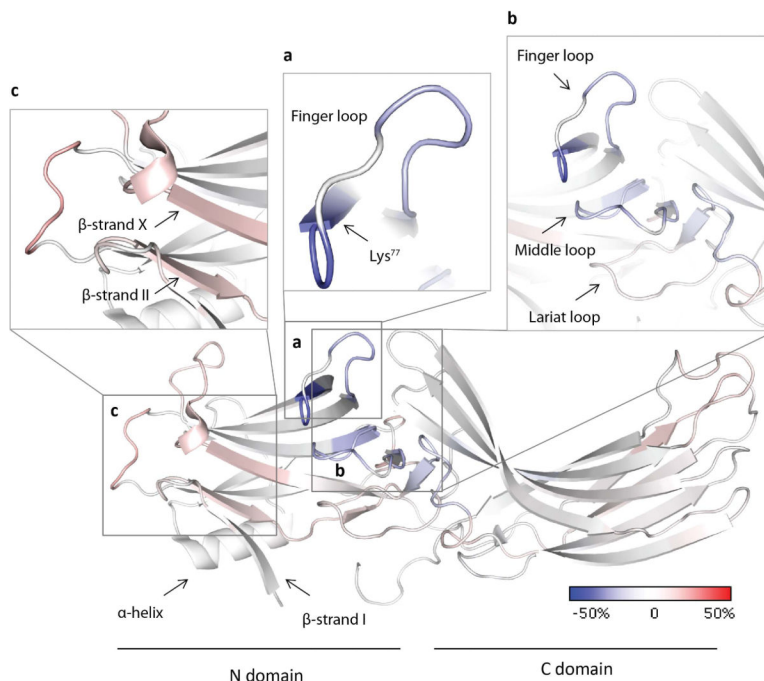
**Figure 2. Hydrogen-deuterium exchange mass spectrometry (HDXMS) analysis reveals potential interface between β₂V₂R and βarr1**

Differential hydrogen-deuterium exchange (HDX) rates of βarr1 in the β₂V₂R-βarr1-Fab30 vs. V₂Rpp-βarr1-Fab30 were mapped on to the βarr1 crystal structure (PDB: 4JQI). Blue and red color coding suggest the βarr1 regions which exchange slower and faster, respectively, in the β₂V₂R-βarr1-Fab30 complex when compared to the V₂Rpp-βarr1-Fab30 complex. Some regions (boxed) with significant HDX rate changes are enlarged in the panels (a)-(c). The HDX rates of the finger loop (residues 63-75) (a), middle loop (residues 129-140) (b) and lariat loop (residues 274-300) (b) became slower, whereas those of other regions, for example, (c) the β-strand I (βI), II (βII) and X (βX) in the N-domain became faster in the β₂V₂R-βarr1-Fab30 complex when compared to the V₂Rpp-βarr1-Fab30 complex.
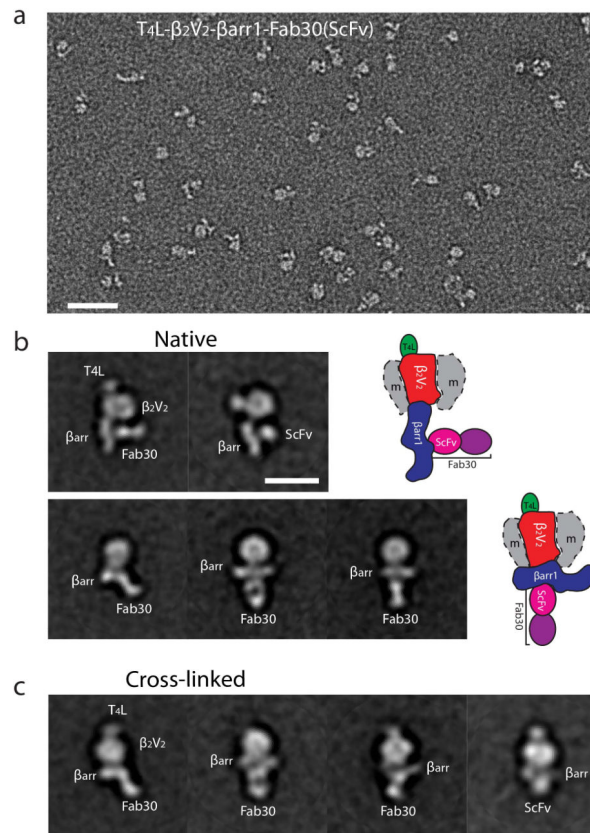
**Figure 3. Single particle EM analysis of the $\beta_2V_2R$-$\beta arr1$-Fab30/ScFv30 complex**
**a.** Representative raw EM image of negative stained T4L-$\beta_2V_2R$-$\beta arr1$-Fab30/ScFv30 complexes. Scale bar = 25 nm. **b.** Representative class averages of the native T4L-$\beta_2V_2R$-$\beta arr1$-Fab30/ScFv30 complex. Class averages of particles displaying the loose "hanging" interaction (top) and the fully engaged "tight" interaction (bottom) are presented. Scale bar = 10 nm. **c.** Representative class averages of the "on-column" cross-linked T4L-$\beta_2V_2R$-$\beta arr1$-Fab30/ScFv30 complex. Upon cross-linking, the majority of class averages display the "tight" (fully engaged) $\beta arr1$ conformation, similar to a fraction (~37%) of particles observed in the non-cross-linked complex.
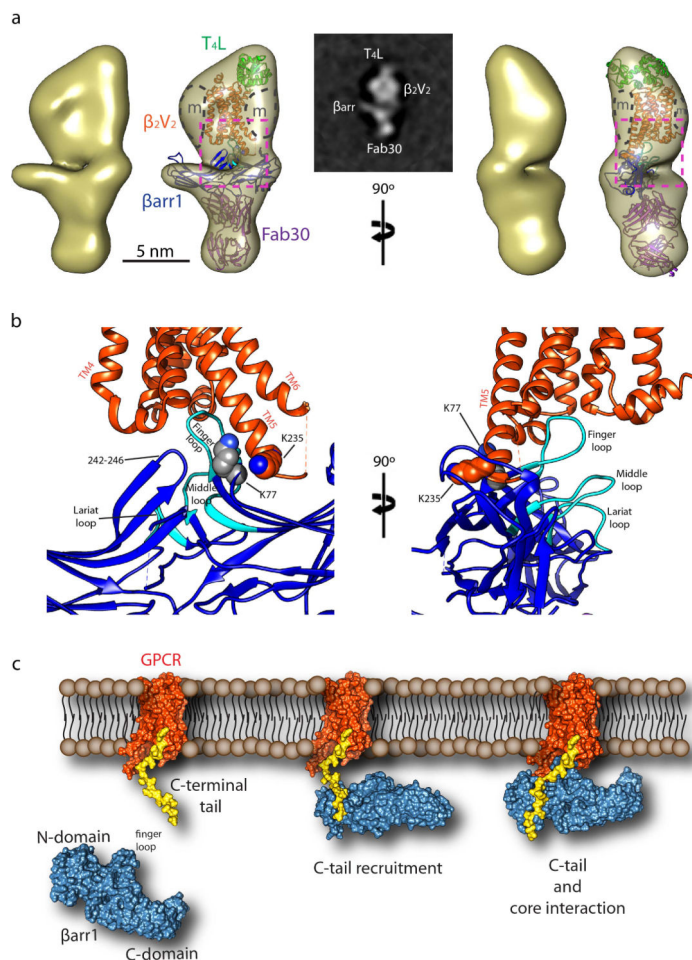
**Figure 4. Structural model of the $\beta_2V_2R$-$\beta$arr1-Fab30 complex**

**a.** Views of the T4L-$\beta_2V_2R$-$\beta$arr1-Fab30 complex 3D reconstruction with modeled T4L-$\beta_2$AR (green-orange, pdb: 3SN6), $\beta$arr1 (blue, pdb: 4JQI), and Fab30 (purple, pdb: 4JQI) crystal structures. The density surrounding $\beta_2V_2R$ represents the LMNG detergent micelle and is marked by "m". **b.** Views of the $\beta_2V_2R$-$\beta$arr1 interface within the dashed line square of panel (a). Areas of $\beta$arr1 with reduced deuterium exchange are shown in cyan. Cross-linked $Lys^{235}$ of $\beta_2V_2R$ and $Lys^{77}$ of $\beta$arr1 are highlighted. **c.** Illustration of the two-step GPCR-$\beta$arr1 interaction using surface representations of the structures of $\beta_2$AR (orange), the phosphorylated C-terminal tail of $V_2R$ (yellow) and $\beta$arr1 (blue). The C-terminal portion of the $V_2R$ peptide ($Glu^{355}$ - $Asp^{367}$) in the right model is positioned as found in the $\beta$arr1-Fab30-$V_2$Rpp structure (pdb:4JQI), whereas the N-terminal portion ($Ala^{342}$ – $Pro^{352}$) was remodeled to connect to the $\beta_2$AR C-terminus.
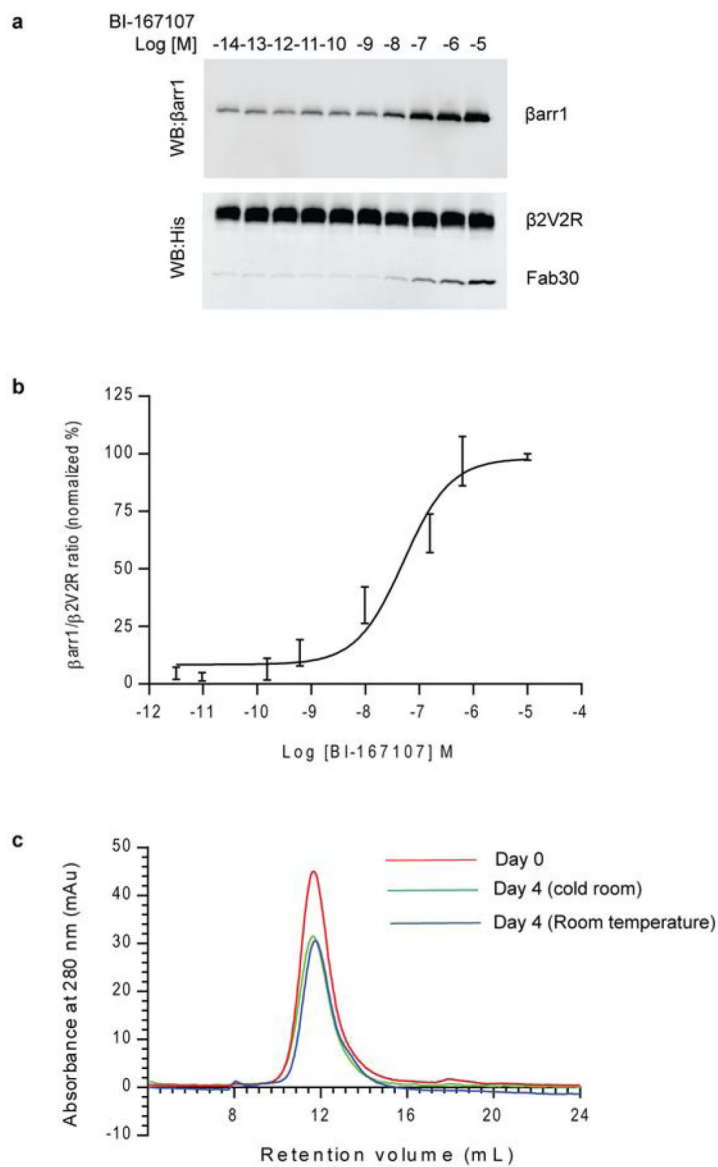
**Extended Data Figure 1. Formation of the β2V2R-βarr1-Fab30 complex follows agonist occupancy of the receptor and it is biochemically stable**

a. Sf9 cells co-expressing the β2V2R, βarr1 and GRK2CAAX were stimulated with varying doses of high affinity agonist BI-167107 followed by addition of Fab30 and purification of the complexes. Stimulation of cells with increasing concentration of BI-167107 results in increasing amount of βarr1 co-purification indicating a direct correlation between occupancy of the receptor with agonist and complex formation. b. Quantification of agonist dependent complex formation from seven independent experiments normalized with respect to βarr1 signal at highest agonist concentration. c. Purified T4L-β2V2R-βarr1-Fab30 complex was stored either at 4°C or at room temperature for 4 days followed by size exclusion chromatography on a superdex 200 (10/300) column (flow rate 0.5 ml/min). No significant dissociation of the complex was detected as monitored by appearance of a peak corresponding to the receptor (13.5 ml) or βarr1 (14.5 ml).
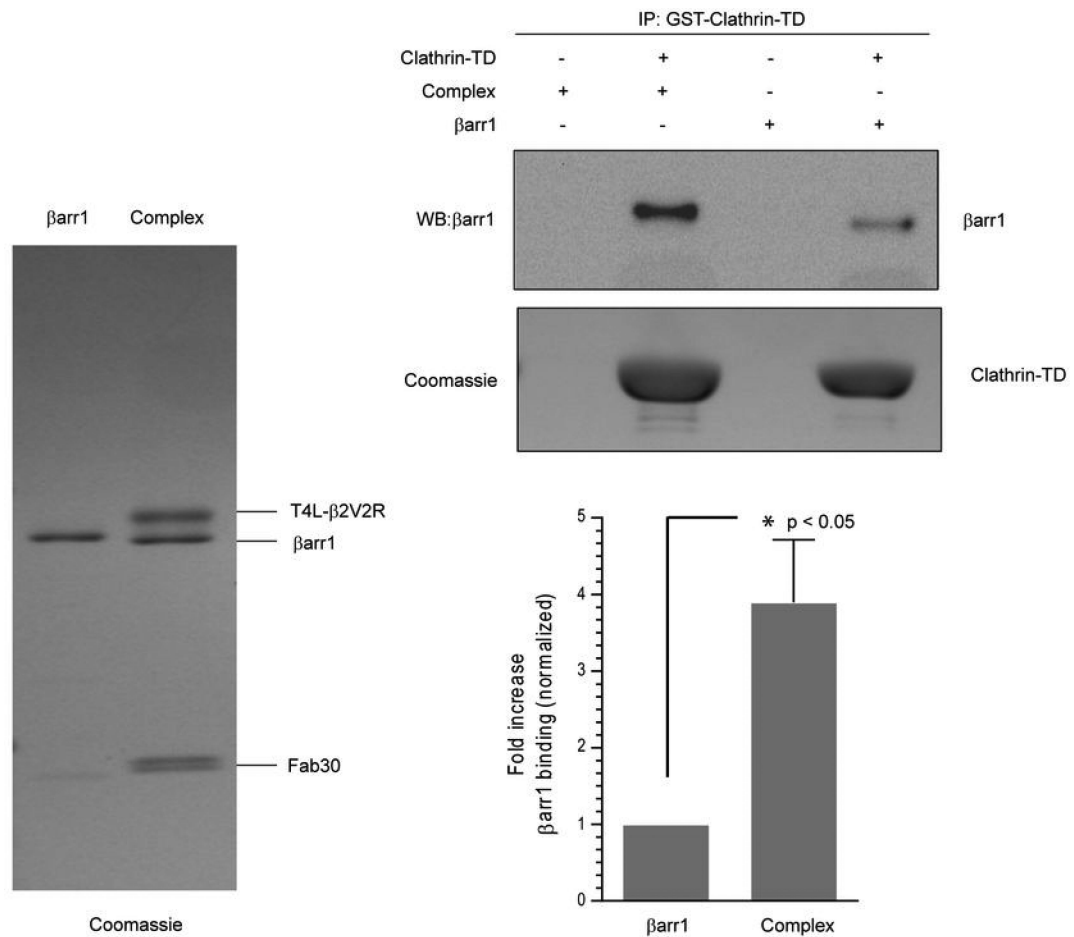
**Extended Data Figure 2. Functionally relevant conformation of βarr1 in the T4L-β2V2R-βarr1-Fab30 complex as revealed by enhanced clathrin -terminal domain (clathrin TD) interaction**
Purified GST (glutathione S-transferase) tagged clathrin-TD was added to the purified complex or equivalent amount of βarr1 alone. Interaction of clathrin-TD with the complex or βarr1 was measured by subsequent co-immunoprecipitation and Western blot analysis. Quantification of four independent experiments shown as a bar graph. The relative intensities of the βarr1 bands are normalized with respect to βarr1 alone (set as 1). A coomassie stained gel indicating comparable amounts of βarr1 for complex vs. βarr1 alone conditions in clathrin-TD coimmunoprecipitation experiments is shown on the left. Errror bar shows SEM. p<0.05 for paired t-test.
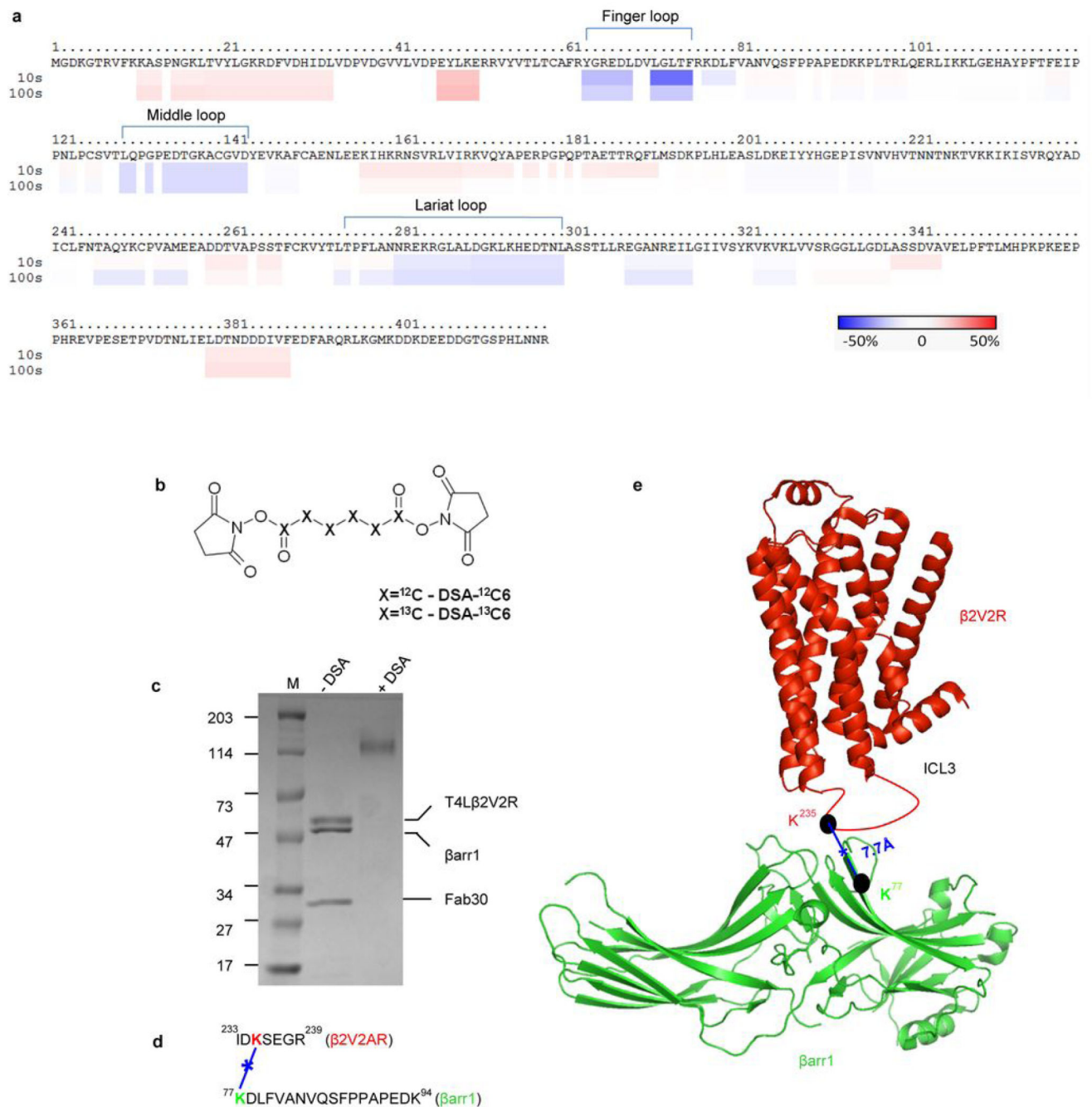
**Extended Data Figure 3. HDXMS analysis and mass-spectrometry based mapping of the cross-linking site in T4L-β2V2R-βarr1-Fab30 complex.**

a. The differential H/D exchange between the T4Lβ2V2R-βarr1-Fab30 complex and the V2Rpp-βarr1-Fab30 complex are mapped on the sequence of βarr1. b. Disuccinimidyl adipate (DSA), a homobifunctional amine-reactive crosslinker) was used to cross-link the pre-formed T4L-β2V2R-βarr1-Fab30 complex. c. A representative SDS-PAGE showing the DSA cross-linking efficiency of the pre-formed complex. d. The cross-linked peptides were characterized with "doublet" peak signatures in mass spectra as described in the methods section and revelaed a cross-link between K235 of the β2V2R and K77 at the distal end of

the finger loop in βarr1. e. Structural model of the β2V2R-βarr1complex highlighting the cross-linking site.
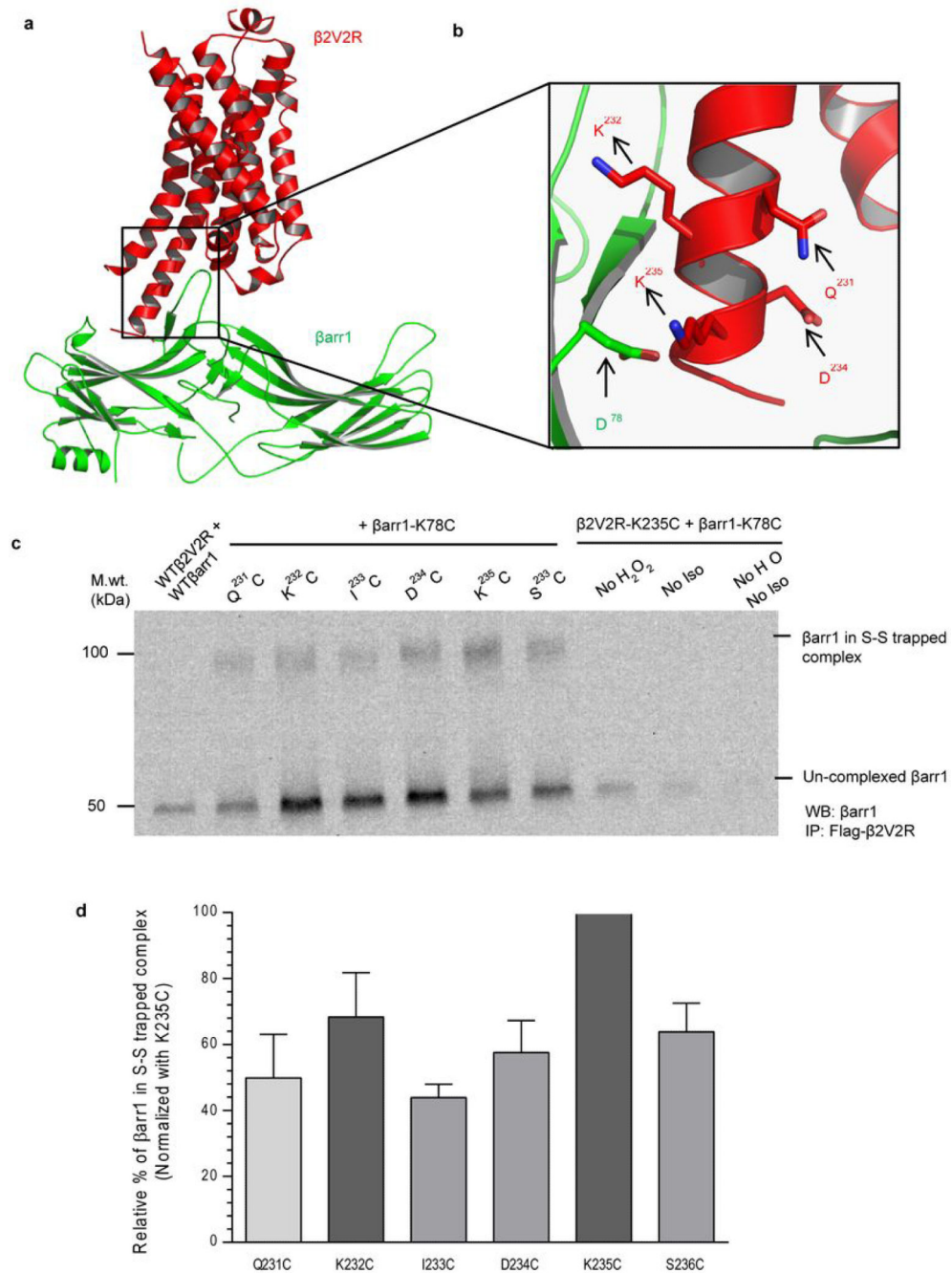
**Extended Data Figure 4. Disulphide trapping strategy reveals close proximity of residue 235 of the β2V2R and residue 78 at the distal end of the finger loop in βarr1.**

a. Structural model of the β2V2R-βarr1 complex depicting the proximity of K235 on the β2V2R and D78 on βarr1. b. Single cysteine insertion mutants of the β2V2R (covering residues 231- 236 ) and βarr1D78C were co-transfected in HEK-293 cells and complex formation was induced by stimulating the cells with an oxidizing agent H2O2 and agonist (Isoproterenol; Iso). Subsequenlty, a co-immunoprecipitation assay was performed using FLAG M2 beads (FLAG-βarr1). Formation of disulphide trapped complex was visualized by

Western blotting. c. Quantification of βarr1 in S-S trapped complex from three indepdent experiments with standard error of the mean.
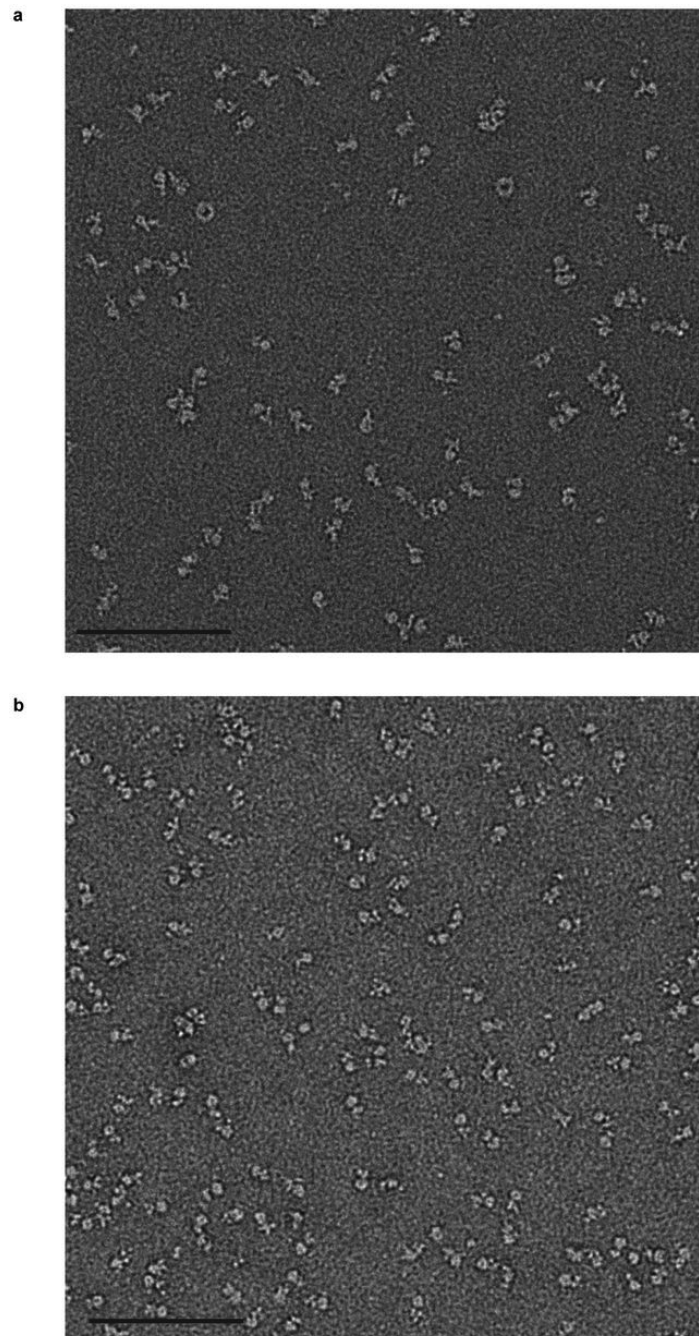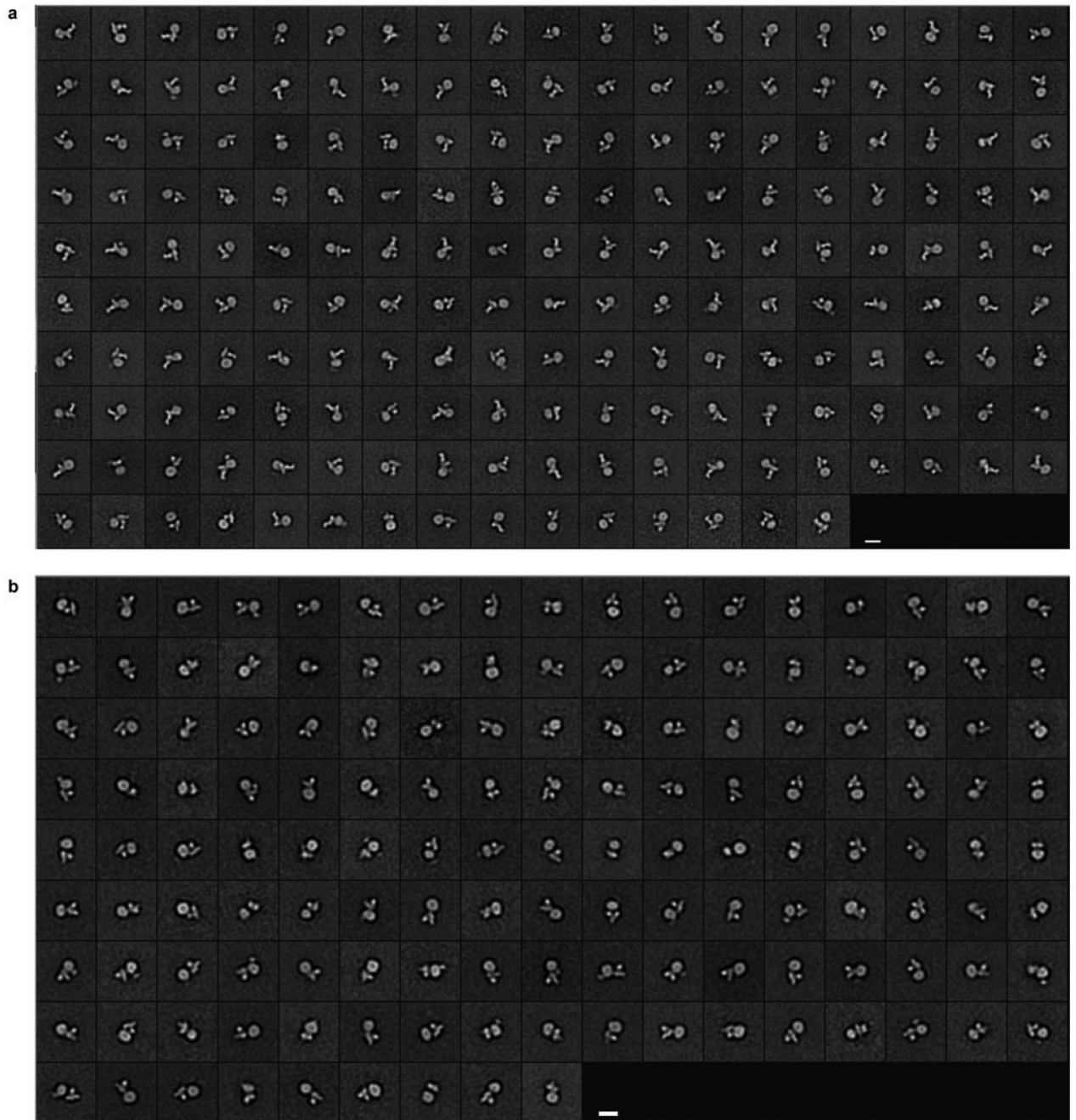
**Extended Data Figure 5. Raw EM images of negative stained native T4L-β2V2R-βarr1-Fab 30(ScFv30) complex.**
a) Raw EM image of T4L-β2V2R-βarr1-Fab30 complex.b) Raw EM image of T4L-β2V2R-βarr1-ScFv30 complex. Scale bar = 100 nm.

**Extended Data Figure 6. 2D classifications of the T4L-β2V2R-βarr1-Fab30(ScFv30) complex. Reference-free 2D class averages were obtained using ISAC.**
a) 2D classification of the T4L-β2V2R -βarr1-Fab30 comple x. b) 2D classification of the T4L-β2V2R-βarr1-ScFv30 complex. Scale bar = 10 nm.
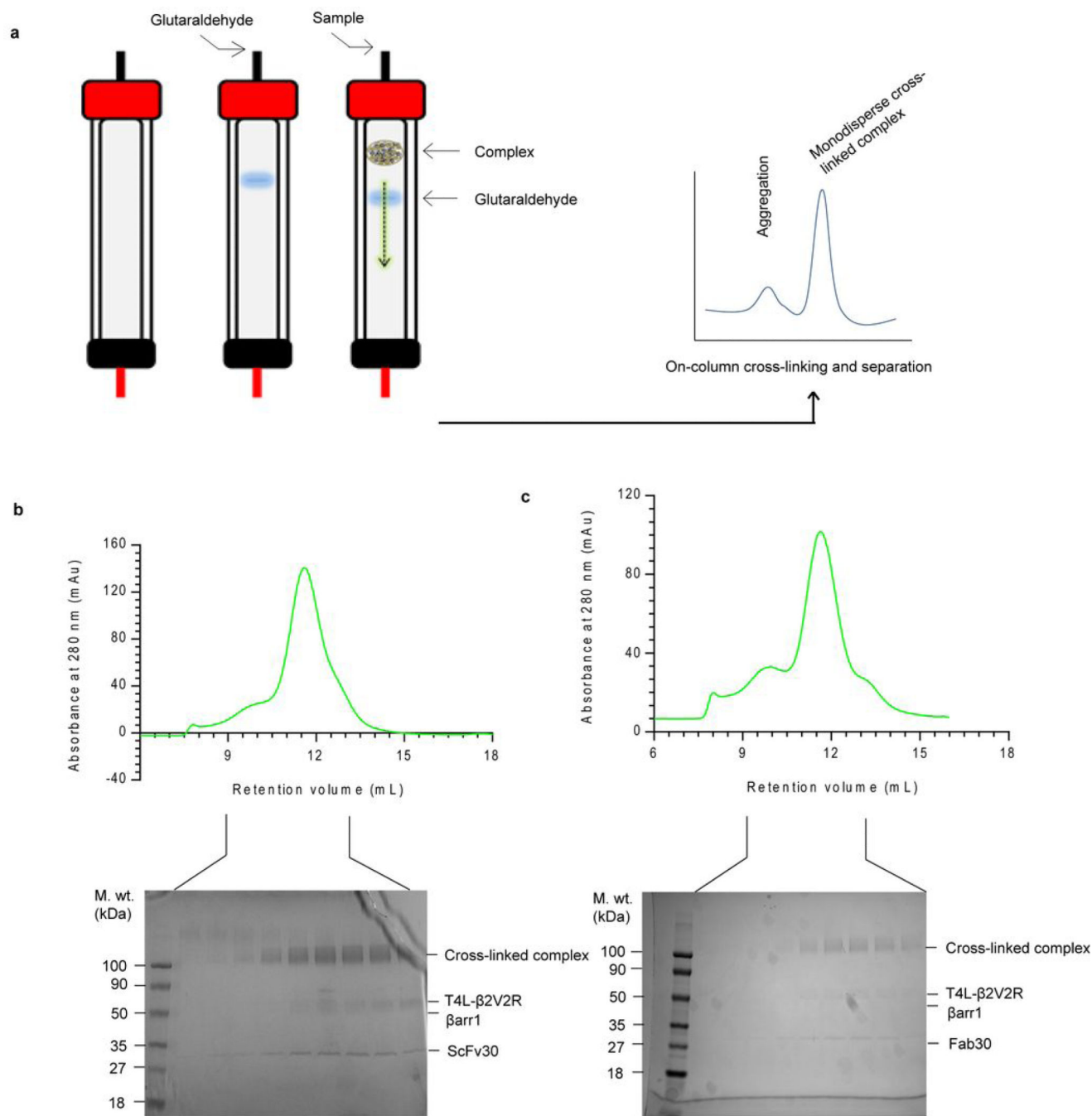
**Extended Data Figure 7. "On-column" glutaraldehyde cross-linking of the pre-formed complex.**
a. Schematic representation of the "on-column" cross-linking strategy. A glutaraldehyde
solution is injected to a size exclusion chromatography column, followed by injection of the
purified complex protein. As the complex protein passes through the glutaraldehyde bolus,
the receptor and the βarr components of the complex are cross-linked through proximal
primary amine groups. This procedure allows only brief exposure of the complex to
glutaraldehyde and serves as an "in-line" purification of homogenously cross-linked protein
from any aggregation that may arise from non-specific cross-linking. b. "On-column" cross-

linking of the T4L-β2V2R-βarr1-ScFv30 complex. Purified complex (approximately 20μM) was injected on to a 24mL Superdex 200 gel filtration column after a pre-injection of 200μL of 0.25% glutaraldehyde bolus. Individual fractions were collected and analyzed by "Simplyblue" stained SDS-PAGE. c. "On-column" cross-linking of the T4L-β2V2R-βarr1-Fab30 complex performed as described for the ScFv complex above.
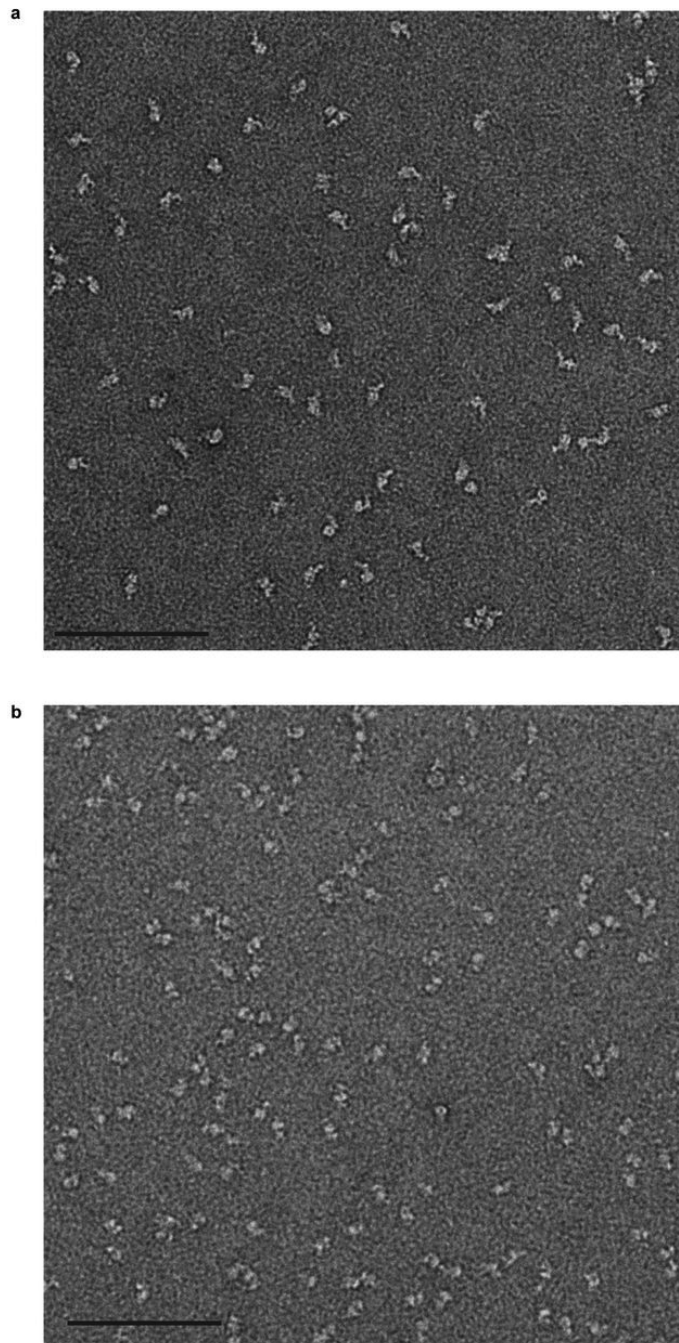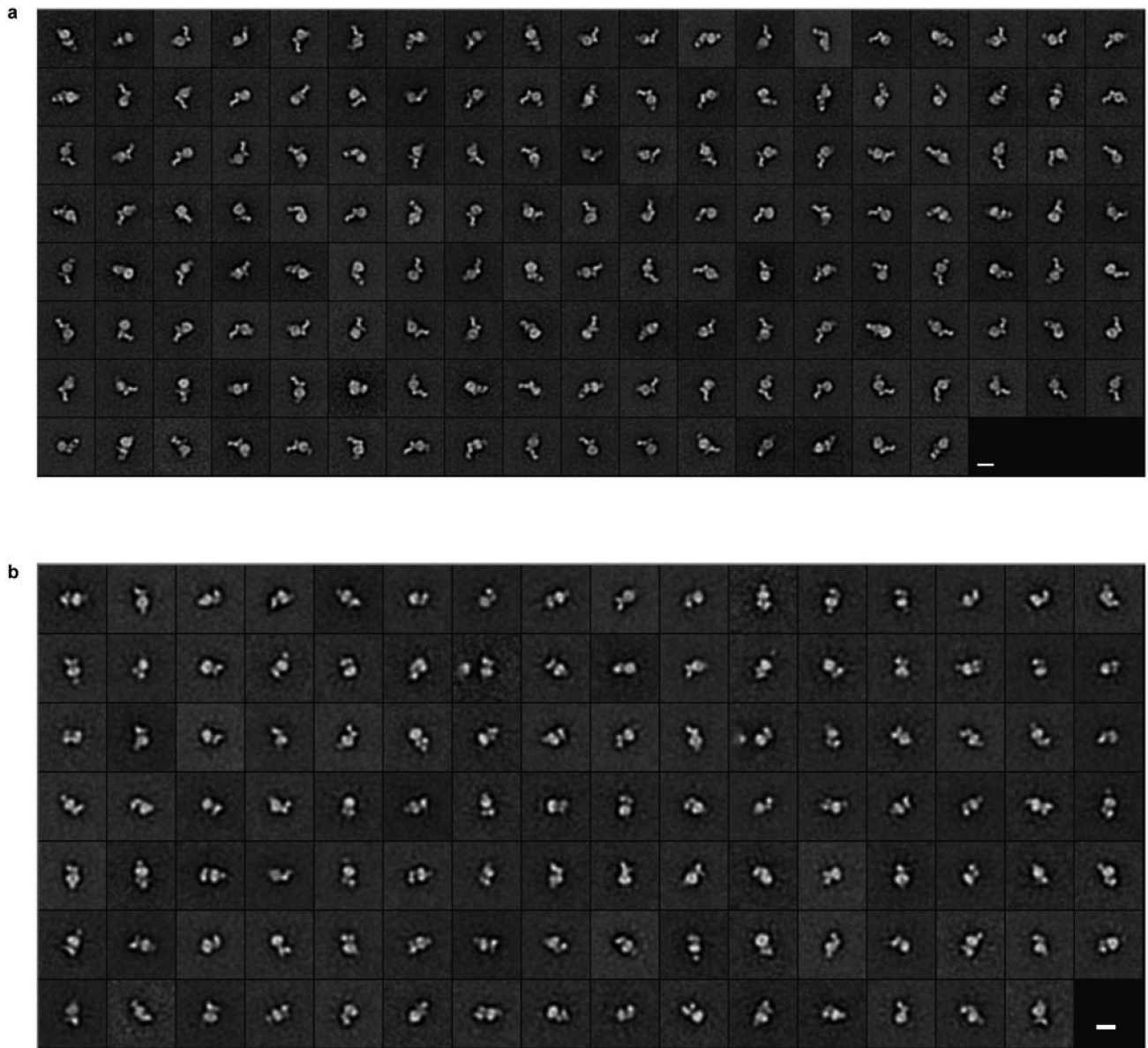
**Extended Data Figure 8. Raw EM images of negative stained cross-linked T4L-β2V2R-β arr1-Fab30(ScFv30) complex.**
a) Raw EM image of T4L-β2V2R-βarr1-Fab30 complex. b) Raw EM image of T4L-β2V2R-βarr1-ScFv30 complex. Scale bar = 100 nm.

**Extended Data Figure 9. 2D classifications of cross-linked T4L-β2V2R-βarr1-Fab30(ScFv30) complex.**
Reference-free 2D class averages were obtained using ISAC. a) 2D classification of cross-linked T4L-β2V2R-βarr1-Fab30 complex. b) 2D classification of cross-linked T4L-β2V2R-βarr1- ScFv30 complex. Scale bar = 10 nm.
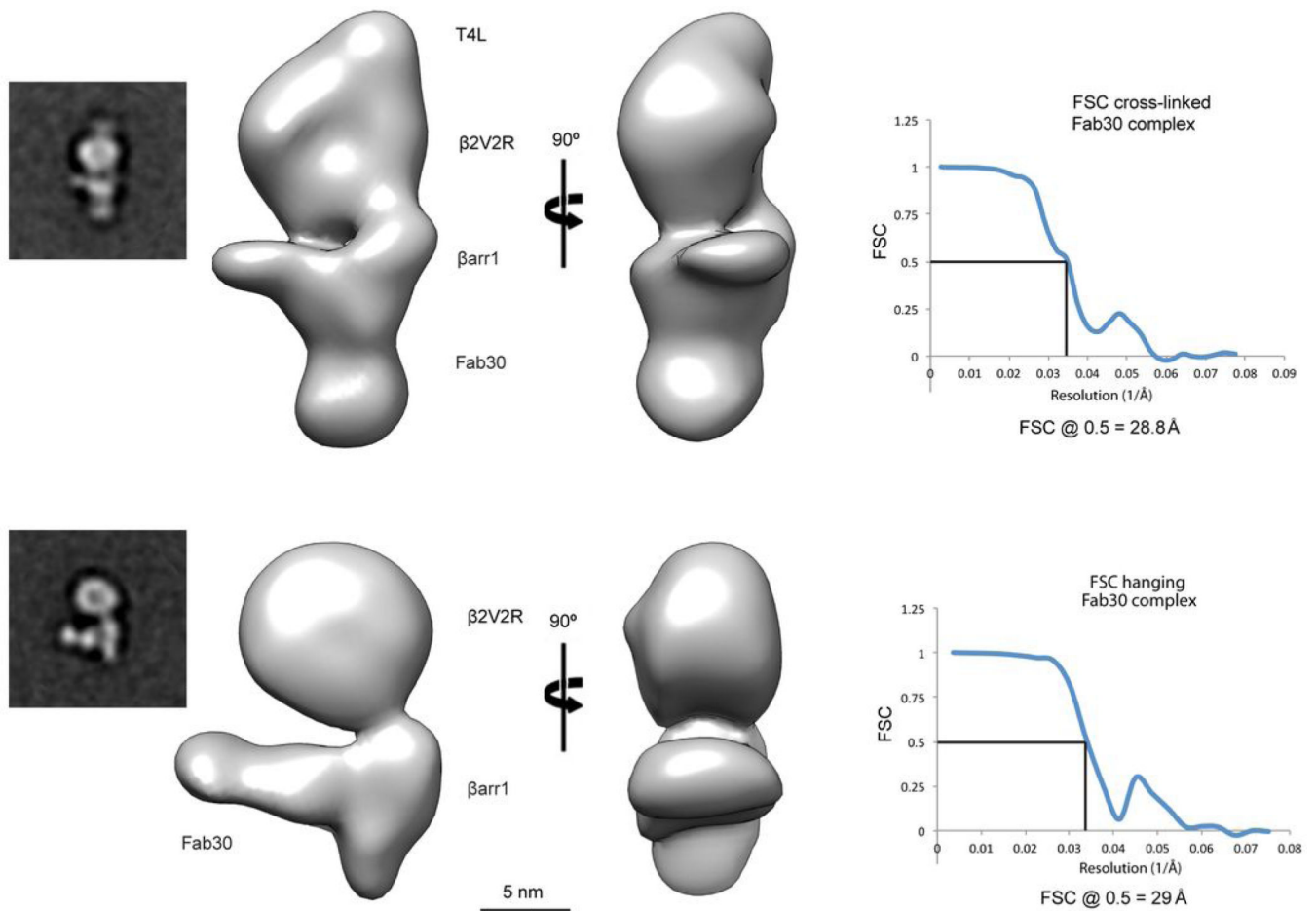
**Extended Data Figure 10. 3D EM reconstructions and resolution indications by Fourier Shell Correlation (FSC) curves.**

The top panel shows the 3D map from particles representing the fully engaged β2V2R-βarr1 conformation of the T4L-β2V2R-βarr1- Fab30 complex. The bottom panel shows the 3D reconstruction from particles displaying the loose, hanging arrestin, conformation of the same complex. Representative 2D averages of particles used for the calculation of initial models by the random conical tilt method are shown on the left of each respective 3D map.